TECHNICAL REPORTS

nature medicine

In vivo imaging of siRNA delivery and silencing in tumors

Zdravka Medarova[1,3], Wellington Pham[1,3], Christian Farrar[1], Victoria Petkova[2] & Anna Moore[1]

With the increased potential of RNA interference (RNAi) as a therapeutic strategy, new noninvasive methods for detection of siRNA delivery and silencing are urgently needed. Here we describe the development of dual-purpose probes for *in vivo* transfer of siRNA and the simultaneous imaging of its accumulation in tumors by high-resolution magnetic resonance imaging (MRI) and near-infrared *in vivo* optical imaging (NIRF). These probes consisted of magnetic nanoparticles labeled with a near-infrared dye and covalently linked to siRNA molecules specific for model or therapeutic targets. Additionally, these nanoparticles were modified with a membrane translocation peptide for intracellular delivery. We show the feasibility of *in vivo* tracking of tumor uptake of these probes by MRI and optical imaging in two separate tumor models. We also used proof-of-principle optical imaging to corroborate the efficiency of the silencing process. These studies represent the first step toward the advancement of siRNA delivery and imaging strategies, essential for cancer therapeutic product development and optimization.

RNA interference has emerged as one of the most promising platforms for therapeutic product development. Its broad applicability, high efficiency[1] and specificity[2,3] could be used to develop a powerful new treatment paradigm with global relevance to any disease amenable to manipulation at the gene expression level.

The biggest obstacle to developing siRNA-based therapies, however, is the delivery of the siRNA molecule to the target tissue. There have been numerous reports of *in vivo* gene silencing with siRNAs, including hydrodynamic injection of synthetic siRNA (refs. 4,5), delivery using lipid-based agents[6–8] and various carriers, such as atelocollagen[9], a protamine-antibody fusion protein[10] and polyethyleneimine[11], as well as local administration[12–14]. Clearly, major prerequisites for the *in vivo* applicability of siRNAs include efficient transfer across the cell membrane, favorable blood half-life and adequate tissue bioavailability, as well as stability of the siRNA. Additionally, for clinical applicability, these requirements need to be achieved in the context of minimally invasive administration. Also, in order to conceive and optimize experimental treatment strategies, there needs to be a way to noninvasively assess siRNA delivery to tissues of interest—using clinically relevant imaging paradigms. At present, reports of the *in vivo* imaging of siRNA in target tissues are limited to bioluminescence imaging of siRNA-mediated silencing[9,15]. The assessment of siRNA delivery, however, is currently based only on *ex vivo* studies.

Here we describe the synthesis and characterization of a new dual-purpose probe for the simultaneous noninvasive imaging and delivery of siRNAs to tumors. This probe consisted of magnetic nanoparticles (for MRI) labeled with Cy5.5 dye (for NIRF) and conjugated to a synthetic siRNA duplex targeting a gene of interest. In addition, the probe was modified with myristoylated polyarginine peptides (MPAP) serving as a membrane translocation module. In a series of experiments targeting model (green fluorescent protein, GFP) and therapeutic (survivin) genes, we found that the delivery of the probe could be monitored *in vivo* by MRI and optical imaging. In addition, we were able to follow the silencing process by optical imaging and to correlate it with histological data. Overall, this new approach could advance siRNA targeting and potential therapy.

RESULTS

Chemical synthesis and characterization of the probe

We synthesized a probe for siRNA delivery and imaging using dextran-coated superparamagnetic nanoparticles, modified with Cy5.5 optical dye and MPAP peptides. We then attached synthetic siRNA molecules targeting GFP-expressing tumors as a model gene to this core (**Fig. 1a**). Tumors stably expressing red fluorescent protein (RFP) served as a control in our studies.

The synthesis of the GFP-targeting complex, MN-NIRF-siGFP, resulted in triple-labeled nanoparticles that had on average three Cy5.5, four MPAP and five siRNA molecules per magnetic nanoparticle (**Fig 1b**).

To quantify the uptake and silencing efficiency of MN-NIRF-siGFP in tumor cells *in vitro*, we incubated 9L-GFP and control 9L-RFP glioma cells with increasing amounts of the probe. After 48 h, we observed a linear, concentration-dependent rise in Cy5.5 fluorescence, reflecting increased uptake of the probe by the cells ($R^2 = 0.97$, **Fig. 2a**). In addition, the presence of the MPAP membrane translocation peptide markedly increased cellular uptake of the probe, compared to that in the control lacking the peptide (**Supplementary**

[1]Massachussetts General Hospital/Massachusetts Institute of Technology/Harvard Medical School Athinoula A. Martinos Center for Biomedical Imaging, Department of Radiology, Massachusetts General Hospital/Harvard Medical School, Room 2301, Building 149, 13th Street, Charlestown, Boston, Massachusetts 02129, USA. [2]Beth Israel Deaconess Medical Center, Harvard Medical School, Room 1034, 77 Louis Pasteur Avenue, Boston, Massachusetts 02215, USA. [3]These authors contributed equally to this work. Correspondence should be addressed to A.M. (amoore@helix.mgh.harvard.edu).

Received 8 August 2006; accepted 24 August 2006; published online 25 February 2007; doi:10.1038/nm1486

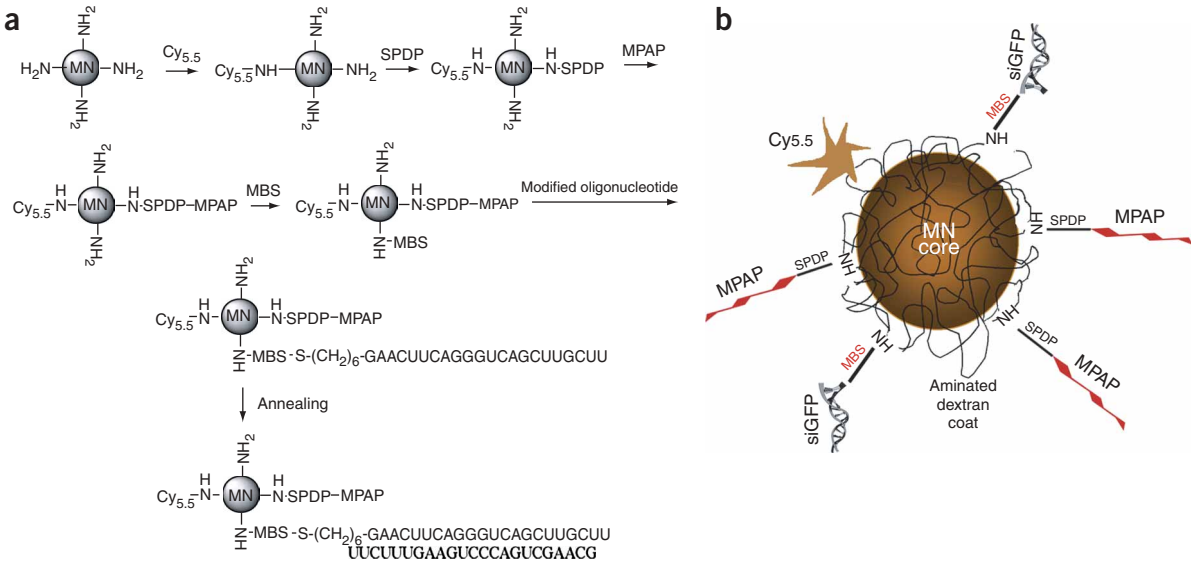

Figure 1 Synthesis of MN-NIRF-siGFP. (**a**) Step-by-step synthesis of the MN-NIRF-siGFP probe, by the sequential conjugation of three different entities onto magnetic nanoparticles. (**b**) The resultant probe consisted of magnetic nanoparticles labeled with near-infrared Cy5.5 dye (NIRF) and linked through two different linkers to membrane translocation peptides (MPAP) and siRNA molecules targeting GFP (siGFP).

Fig. 1 online). The silencing efficiency in 9L-GFP cells was manifested by a concentration-dependent decrease in GFP fluorescence (R^2 = 0.97, **Fig. 2a**), which was most pronounced at 48 h. By contrast, this trend was not observed in 9L-RFP cells (data not shown).

We corroborated these results by confocal microscopy. Following a 48-h incubation with MN-NIRF-siGFP, there was extensive cytoplasmic Cy5.5 fluorescence in both 9L-GFP and 9L-RFP cells, indicating the presence of the probe, with an apparent predominance in perinuclear regions (**Fig. 2b**). Earlier reports have shown a similar localization of siRNA conjugates, presumably as a result of sequestration by the RNA-induced silencing complex (RISC)[8,16,17]. In 9L-GFP cells, however, incubation with the probe resulted in a marked suppression of GFP fluorescence, whereas in 9L-RFP cells RFP fluorescence remained at preincubation levels (**Fig. 2b**). These results indicated that the silencing effect mediated by the MN-NIRF-siGFP probe was specific for 9L-GFP cells.

In vivo imaging of MN-NIRF-siGFP delivery and silencing

We monitored the delivery of the probe to tumors by *in vivo* MRI of mice bilaterally implanted with 9L-GFP and 9L-RFP tumors before and 24 h after intravenous injection of the probe. Superparamagnetic iron oxide nanoparticles are characterized by their strong T2 magnetic susceptibility effects. Their presence in tissue was reflected by a marked decrease of T2 relaxation times, resulting in a loss of signal (darkening) on magnetic resonance images. As expected, tumors appeared characteristically bright on T2 images acquired before administration of the contrast agent. Images acquired after administration of the contrast agent showed a significant drop in T2 relaxivity in the tumors (P = 0.0012 for 9L-GFP, P = 0.0049 for 9L-RFP), as a result of accumulation of MN-NIRF-siGFP. By contrast, the T2 relaxation times of control muscle tissue remained unchanged (**Fig. 3a**). We also confirmed delivery of MN-NIRF-siGFP to tumors by *ex vivo* high-resolution MRI. Distinct foci of signal loss, reflecting probe accumulation, were easily identifiable in tumors derived from mice injected with the probe but not from those in controls injected

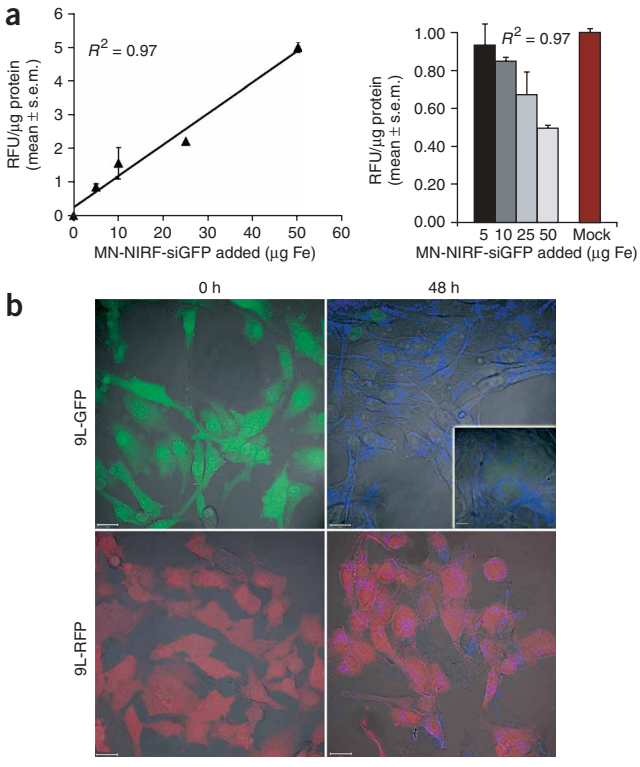

Figure 2 *In vitro* testing of MN-NIRF-siGFP cell uptake and silencing efficiency in stably transfected 9L-GFP gliosarcoma cells. (**a**) Quantitative studies. MN-NIRF-siRNA uptake, as estimated by Cy5.5 fluorescence, increased in a linear, concentration-dependent fashion (left). The silencing effect was manifested as a concentration-dependent decrease in GFP relative fluorescence levels (right). Data represent an average of three experiments. RFU, relative fluorescence units. (**b**) Confocal microscopy showing MN-NIRF-siGFP accumulation in 9L-GFP and 9L-RFP cells. Note that although the probe accumulated in both cell lines (Cy5.5 fluorescence, blue), there was a substantial silencing effect in the 9L-GFP cell line, resulting in marked suppression of GFP fluorescence. Scale bar, 20 μm.

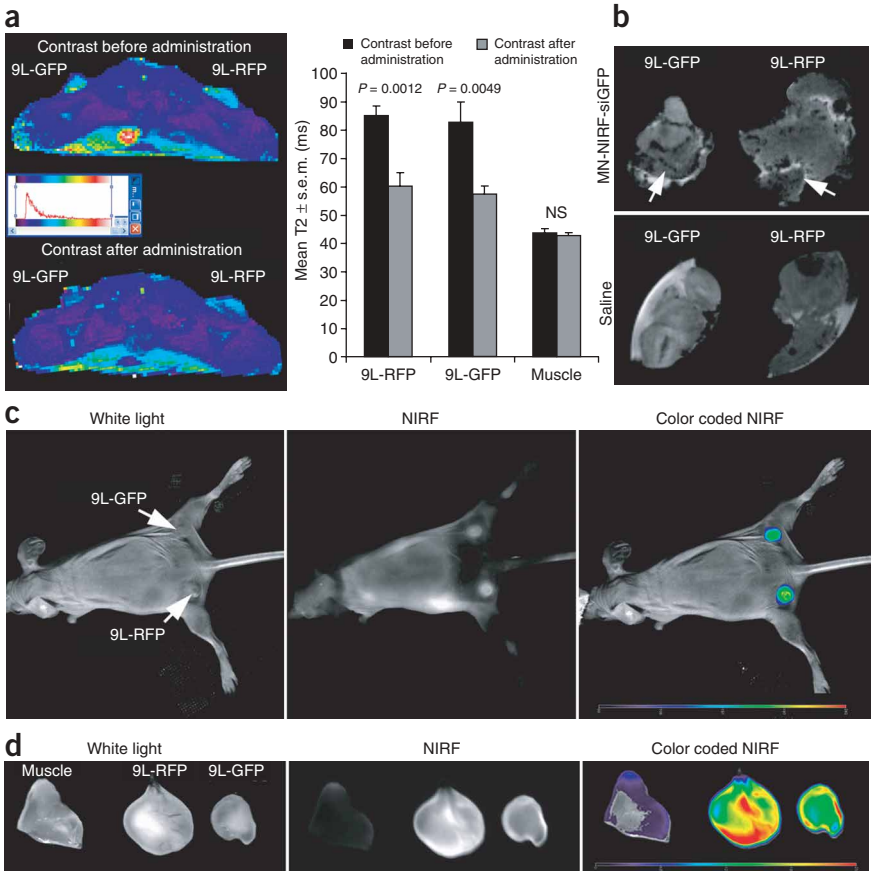

Figure 3 *In vivo* imaging of MN-NIRF-siGFP delivery to tumors. (**a**) *In vivo* MRI was performed on mice bearing bilateral 9L-GFP and 9L-RFP tumors before and 24 h after MN-NIRF-siGFP administration. After injection of the probe, there was a significant drop in T2 relaxivity associated with the tumors. Note that T2 relaxation times of muscle tissue remained unchanged. (**b**) *Ex vivo* high-resolution MR images of excised tumors (78 μm isotropic). Distinct foci of signal loss (arrows), reflecting probe accumulation, were easily identifiable in tumors derived from mice injected with the probe but not from saline-injected controls. (**c**) *In vivo* NIRF optical imaging of the same mice as in **a** produced a high-intensity NIRF signal associated with the tumors. This confirmed the delivery of the MN-NIRF-siGFP probe to these tissues. (**d**) *Ex vivo* NIRF optical imaging demonstrated a significantly higher fluorescence in tumors than in muscle tissue ($P = 0.0058$).

with saline (**Fig. 3b**). We obtained an independent macroscopic confirmation of probe delivery to the tumors by NIRF of the same mice immediately after each MRI session. The signal in the Cy5.5 channel was detected only after injection of the MN-NIRF-siGFP probe (**Fig. 3c**), not before (data not shown), and was confirmed by *ex vivo* NIRF ($P = 0.0058$, **Fig. 3d**).

In vivo biodistribution of MN-NIRF-siGFP showed appreciable accumulation in both tumors (**Supplementary Fig. 2** online). The rest of the organs showed accumulation consistent with the literature on related iron oxide nanoparticles[18,19] and their metabolic processing[20]. Taken together, these results indicate that the MN-NIRF-siGFP probe was successfully delivered to tumors and that this process could be detected by *in vivo* MRI and optical imaging.

We studied the *in vivo* silencing efficiency of the MN-NIRF-siGFP probe by *in vivo* optical imaging in the GFP and RFP channels on mice bearing bilateral 9L-GFP and 9L-RFP tumors, before and 48 h after injection of the probe. There was a drop in 9L-GFP–associated fluorescence 48 h after probe administration (**Fig. 4a**, $P = 0.0083$). We found no corresponding drop in 9L-RFP–associated red fluorescence, suggesting that the effect was GFP specific. We also confirmed the silencing effect of the MN-NIRF-siGFP probe by *ex vivo* optical imaging of excised experimental and control tumors (**Fig. 4b**).

We further validated probe delivery to 9L-GFP and 9L-RFP tumors and silencing efficiency after persistence in the circulation by confocal microscopy 48 h after injection (**Fig. 4c**). Whereas 9L-RFP tumor sections remained brightly fluorescent, 9L-GFP tumors produced only background GFP fluorescence. Evidently, the probe accumulated in both tumors with a heterogeneous pattern, consistent with the innate regional differences in tumor growth rates, vascular density, presence of other tumor-associated cell types and/or vascular permeability. In agreement with the known uptake of dextran-coated iron oxides by tumor-recruited macrophages[19], for example, we observed partial colocalization of MN-NIRF-siGFP with these cells (**Supplementary Fig. 3** online). These data indicated that the probe was not only intravenously delivered to the tumors but also produced a strong specific silencing effect in 9L-GFP tumors.

Finally, as an independent confirmation of the observed *in vivo* effects of MN-NIRF-siGFP silencing, we performed quantitative RT-PCR. *Gfp* mRNA levels in tumors from mice treated with MN-NIRF-siGFP were 85 ± 2% (mean ± s.e.m.; $P < 0.001$) lower than in saline-treated controls and 97 ± 1% ($P < 0.001$) lower than in mismatch-treated controls (**Fig. 4d**). By contrast, 18s rRNA levels remained unchanged. These values are similar to those reported for targets in the liver and kidneys using hydrodynamic injection of comparable amounts of siRNA (refs. 4,13,21).

A major concern related to the *in vivo* delivery of siRNAs deals with the induction of type I interferon and inflammatory cytokines[22–24]. We found no significant increase ($P > 0.05$) in the levels of serum interferon (IFN)-α or inflammatory cytokines (interleukin (IL)-6, tumor necrosis factor) in mice treated with MN-NIRF-siGFP compared to mice injected with the parental unmodified magnetic nanoparticle or to nontreated controls, suggesting the absence of immunostimulatory properties (**Supplementary Fig. 4** online). In addition, we did not find elevated toxicity of MN-NIRF-siGFP in the treated mice, as assessed by monitoring serum aspartate aminotransferase (AST) and alanine aminotransferase (ALT) levels, compared to mice treated with the parental magnetic nanoparticle or to nontreated controls (**Supplementary Fig. 4**). Finally, apoptotic levels in tumors treated with the MN-NIRF-siGFP probe and parental magnetic nanoparticles were comparable (**Supplementary Fig. 4**), indicating the absence of cytotoxicity originating from the probe. This observation was corroborated by the absence of any signs of tumor histopathology in frozen tumor sections stained with hematoxylin & eosin (H&E, **Supplementary Fig. 4**). With these additional results, we feel confident that the observed effects were not the result of cellular toxicity but rather represented gene-specific silencing.

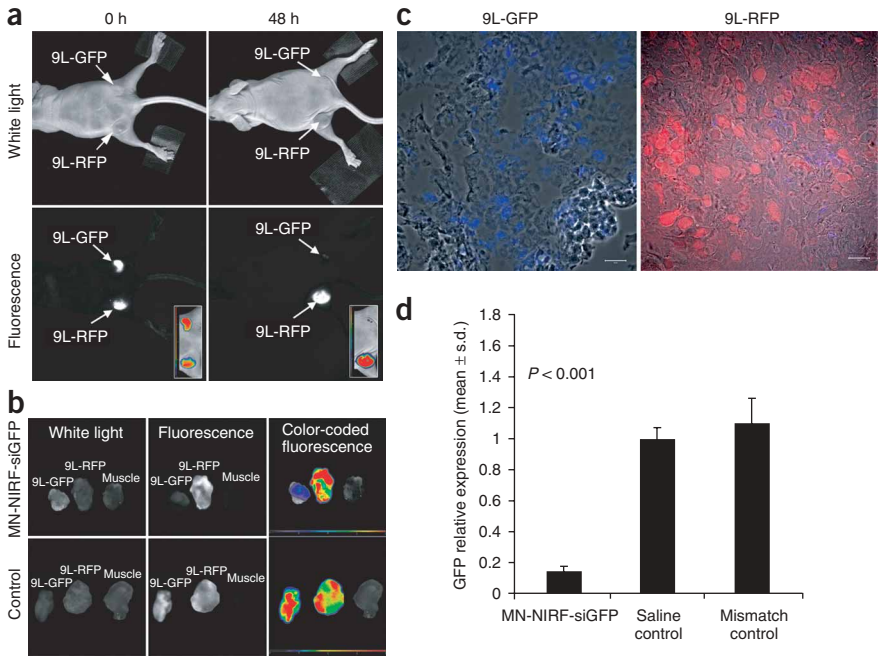

Figure 4 *In vivo* imaging of MN-NIRF-siGFP silencing in tumors. (**a**) *In vivo* NIRF optical imaging of mice bearing bilateral 9L-GFP and 9L-RFP tumors 48 h after intravenous probe injection. There was a marked decrease in 9L-GFP–associated fluorescence ($P = 0.0083$) and no change in 9L-RFP fluorescence. To generate GFP/RFP reconstructions, GFP and RFP images were acquired separately and then merged. (**b**) Correlative *ex vivo* fluorescence optical imaging showed a significant drop in fluorescence intensity in 9L-GFP tumors ($P = 0.0036$). There was no evidence of silencing in saline-injected controls. (**c**) Confocal microscopy of frozen tumor sections indicated the presence of the probe in both 9-GFP and 9L-RFP tumors (blue). However, in GFP tumors, GFP fluorescence was predominantly at background levels. Note that the 9L-RFP section produced bright fluorescence in the red channel. Scale bar, 20 μm. (**d**) Quantitative RT-PCR analysis of GFP expression performed on total RNA extracted from 9L-GFP tumors from mice injected with either MN-NIRF-siGFP, a mismatch control or saline solution. Representative data are shown.

siRNA delivery in a therapeutic tumor model

Having established the feasibility of our imaging and delivery strategy in these initial proof-of-principle experiments, we addressed the issue of gene silencing in a therapeutic scenario. For this purpose, we designed a nanoparticle probe targeting the antiapoptotic gene *Birc5*, which encodes survivin (MN-NIRF-siSurvivin). Survivin is a member of the inhibitor of apoptosis protein (IAP) family, which shows tumor-restricted expression in most human neoplasms and therefore represents an attractive therapeutic target[25].

We administered MN-NIRF-siSurvivin systemically twice a week for 2 weeks to nude mice bearing subcutaneous human colorectal carcinoma tumors (LS174T) with no evidence of IFN-α induction ($P = 0.28$, $n = 3$). On *in vivo* magnetic resonance images, there was a significant drop in tumor-associated T2 relaxation times ($P = 0.003$) after delivery of MN-NIRF-siSurvivin (**Fig. 5a**; confirmed by *in vivo* NIRF imaging, **Fig. 5b**). We detected no NIRF signal in the tumor before administration of the probe (data not shown).

We corroborated specific silencing of survivin by RT-PCR. Survivin transcript levels in tumors treated with MN-NIRF-siSurvivin were 97 ± 2% lower than in controls treated with the parental magnetic nanoparticle ($P < 0.01$, **Fig. 5c**) and 83 ± 2% lower than in mice treated with mismatch control ($P < 0.01$, **Fig. 5c**). This effect was accompanied by a noticeable increase in tumor-associated levels of apoptosis (**Fig. 5d**) and necrosis (**Fig. 5e**) compared to that in controls. These results showed the applicability of the probe in a potential therapeutic scenario.

DISCUSSION

The goal of this study was to design and test a new approach for imaging siRNA delivery and silencing in tumors. The combination of two imaging modalities provided us with the fine resolution (10–100 μm) and unlimited depth penetration of MRI, as well as the high sensitivity (10^{-9} and 10^{-17} moles/l) and short acquisition times of optical imaging[26].

The rationale for using magnetic nanoparticles for tumor imaging is justified by their proven accumulation in tumors, presumably resulting from enhanced permeability and retention (EPR effect[27]) associated with the hyperpermeable tumor vasculature and from increased fluid-phase endocytosis by actively proliferating tumor cells[28]. Therefore, we need to emphasize that MN-NIRF-siRNA does not carry a tumor-targeting moiety, and it is likely that its accumulation in tumors is a reflection of the effects described above. Further enhancement of MN-NIRF-siRNA accumulation in tumors could probably be achieved by conjugation to tumor-specific ligands[18].

In this study we hypothesized that magnetic nanoparticle coupling to a membrane-translocation module would mediate its localization to the cytoplasm, essential for efficient initiation of RNAi by the siRNA duplex. Consequently, our delivery strategy allowed us to achieve substantial silencing in tumors. This effect is comparable or superior to previously published results that have reported levels of silencing ranging between ~50% (ref. 11) and 90% (refs. 4–6,9,13).

We suggest that as the dsRNA molecule is linked to magnetic nanoparticles by a stable thioether bond, it remains tethered to the nanoparticles without compromising silencing efficiency. It has previously been shown that chemical conjugation of the siRNA does not compromise silencing[17,29]. In fact the presence of a carrier not only preserves biological activity but also enhances stability, systemic delivery and *in vivo* potency[30]. In addition, Ambion has announced that double labeling of the sense and antisense strands with Cy3 and the bulky fluorescent dye FITC, respectively, do not compromise siRNA activity (http://www.ambion.com/techlib/tn/93/935.html). We need to emphasize, however, that the precise mechanisms mediating the efficient gene silencing *in vivo* reported here are not fully understood and are currently under detailed investigation.

The combination of the favorable biodistribution of these nanoparticles to tumors and their imaging properties represents an exciting possibility for the simultaneous delivery and detection of siRNA-based therapeutic agents *in vivo*. The feasibility of such studies is underscored by the recent demonstration of substantial silencing in non-human primates following systemic siRNA administration at clinically relevant doses[31]. Overall, we believe that this study represents an important new step toward the application of siRNAs as cancer therapeutic agents by providing a new imaging strategy with which to assess their delivery and silencing.

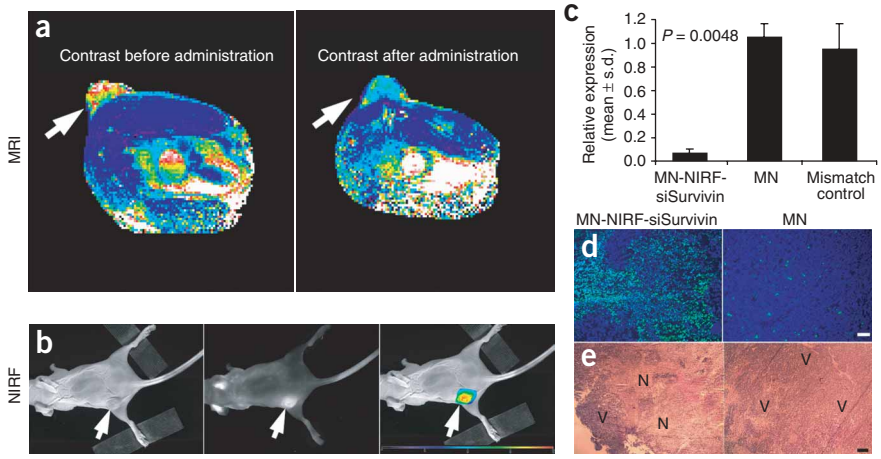

Figure 5 Application of MN-NIRF-siSurvivin in a therapeutic tumor model. (**a**) *In vivo* MRI of mice bearing subcutaneous LS174T human colorectal adenocarcinoma (arrows). There was a significant drop in T2 relaxivity in images acquired after administration of the contrast agent ($P = 0.003$), indicating probe delivery. (**b**) A high-intensity NIRF signal on *in vivo* optical images associated with the tumor following injection of MN-NIRF-siSurvivin confirmed the delivery of the probe to this tissue (left, white light; middle, NIRF; right, color-coded overlay). (**c**) Quantitative RT-PCR analysis of survivin expression in LS174T tumors after injection with either MN-NIRF-siSurvivin, a mismatch control or the parental magnetic nanoparticle (MN). Data are representative of three separate experiments. (**d**) Note distinct areas with a high density of apoptotic nuclei (green) in tumors treated with MN-NIRF-siSurvivin (left). Such areas were not identified in tumors treated with the control magnetic nanoparticles (right). Sections were counter-stained with 6-diamidino-2-phenylindole (DAPI, blue). (**e**) H&E staining of frozen tumor sections revealed considerable eosinophilic areas of tumor necrosis (N) in tumors treated with MN-NIRF-siSurvivin (left). Tumors treated with magnetic nanoparticles were devoid of necrotic tissue (right). Purple hematoxiphilic regions (V) indicate viable tumor tissues. Scale bar, 50 μm.

METHODS

siRNA. The GFP siRNA duplex, directed against the sequence 5′-GCA AGC TGA CCC TGA AGT TC-3′ (refs. 32,33) was designed and synthesized to target 'humanized' GFP (phGFP-S65T, nucleotides 122–141, ref. 34) by Ambion. siRNA to human survivin and mismatch control siRNA were also designed and synthesized by Ambion.

Probe synthesis and characterization. The synthesis of the MN-NIRF-siGFP probe is shown in **Figure 1a**. Briefly, we conjugated Cy5.5 succinimide ester (Amersham Biosciences) to magnetic nanoparticles as previously described[18]. We further conjugated the magnetic nanoparticles with a heterobifunctional cross-linker, *N*-succinimidyl 3-(2-pyridyldithio) propionate (SPDP, Pierce Biotechnology), via the *N*-hydroxy succinimide ester, after purification using a magnetic-activated cell sorting (MACS) column (Miltenyl Biotech). We attached MPAP peptides (Myr-Ala-$(Arg)_7$-Cys-$CONH_2$) to this linker via a sulfhydryl reactive pyridyl disulfide residue in PBS/EDTA, pH 7.0. Finally, we coupled the aminated magnetic nanoparticle with an m-maleimidobenzoyl-*N*-hydroxysuccinimide ester (MBS) crosslinker in PBS, pH 8.5.

We modified the antisense strand of the 22-nucleotide siRNA duplex with a thiol moiety via a hexyl spacer for bioconjugation. Before labeling, we deprotected the disulfide-protecting group on 5′-S-S-$(CH_2)_6$- by resuspending the 5′-S-S-$(CH_2)_6$- modified oligo with 100 mM of tris-(2-carboxyethyl)phosphine hydrochloride (TCEP) in PBS, pH 8.5, for 30 min under argon. We then allowed the free thiol single-stranded RNA to react with the previously activated iron oxide product via the MBS crosslinker. We quantified the labeling ratio based on the provided absorbance and extinction coefficient of 260 nm and 210900/M/cm, respectively. We annealed the oligonucleotides using a 5× annealing buffer as instructed by Ambion. We synthesized MN-NIRF-siSurvivin and the mismatch control siRNA using an analogous procedure.

For the biodistribution studies, we modified the MPAP peptide on MN-NIRF-siGFP to incorporate an additional tyrosine at its carboxy terminus (Myr-Ala-$(Arg)_7$-Cys-Tyr-$CONH_2$) for exchange with ^{125}I. We radioiodinated the resultant probe using the Iodogen method (Pierce). Details on the synthesis are provided in **Supplementary Methods** online.

Cell lines. We maintained stably transfected 9L-GFP (GFP-S65T)[35], 9L-RFP (DsRed2) gliosarcoma cells and human colon adenocarcinoma LS174T cells (ATCC) as recommended by the supplier.

***In vitro* cell uptake studies.** For quantitative determination of probe uptake in 9L-GFP and 9L-RFP gliosarcoma lines, we incubated cells with various amounts (5–50 μg of Fe, 0.22–2.2 nmol RNA) of MN-NIRF-siGFP for up to 48 h at 37 °C in a humidified CO_2 atmosphere. To assess the contribution of the MPAP membrane translocation peptide to cellular uptake, we also incubated 9L-GFP cells with the parental MN-NIRF nanoparticle conjugated to MPAP for 48 h. MN-NIRF nanoparticles lacking MPAP served as control. After extensive washing with HBSS, we lysed the cells in 300 μl of ice-cold lysis buffer (1% Triton X-100, 0.1% BSA) and subjected the cell lysates to fluorescence measurements using a SpectraMax M2 fluorescence spectrophotometer (Molecular Devices). We normalized fluorescence intensity to total protein, determined by BCA assay (Pierce Biotechnology). These values were then normalized to those observed in the absence of siRNA (mock).

Fluorescence confocal microscopy and histology. We performed fluorescence confocal microscopy of 9L-GFP and 9L-RFP tumor cells. Cells were incubated with MN-NIRF-siGFP (25 μg Fe, 1.1 nmols RNA) for 48 h at 37 °C and imaged by microscopy in the FITC channel (GFP detection, 9L-GFP), the Cy3 channel (RFP detection, 9L-RFP) and the Cy5.5 channel (MN-NIRF-siGFP detection). We used Nomarski Optics (for cellular and tissue definition) Imaging was performed using an Axiovert 200M inverted microscope (Carl Zeiss) equipped with an LSM Pascal Vario RGB Laser Module (Arg 458/488/514 nm, HeNe 543 nm, HeNe 633 nm). For macrophage staining, we incubated frozen tumor sections with a rat primary antibody to mouse CD68 (FA-11) (Serotec) followed by a rhodamine-labeled goat secondary antibody to rat IgG (Abcam). We color-coded the final images blue for Cy5.5 (MN-NIRF-siGFP) and red for rhodamine (macrophages).

***In situ* detection of cell death.** To evaluate levels of apoptosis in tumors, we performed a TUNEL assay on 7-μm-thick frozen tumor sections (Apoptag fluorescein *in situ* apoptosis detection kit, Chemicon) according to the manufacturer's protocol. We counterstained the nuclei with VECTASHIELD mounting medium with DAPI (Vector). We stained consecutive sections with H&E and analyzed them by light microscopy for histopathology.

Analysis of liver toxicity and cytokines. We analyzed levels of serum aspartate aminotransferase (AST), alanine aminotransferase (ALT) and serum cytokine according to manufacturers' protocols. Details in **Supplementary Methods**.

TaqMan real-time quantitative RT-PCR. We extracted total RNA from tumors injected with MN-NIRF-siGFP and from control 9L-GFP tumors, using the Rneasy Mini kit according to the manufacturer's protocol (Qiagen). We determined relative levels of *Gfp* mRNA by real-time quantitative RT-PCR (TaqMan protocol). We performed TaqMan analysis using an ABI Prism 7700 sequence detection system (PE Applied Biosystems). We designed the PCR primers and TaqMan probe specific for *Gfp* mRNA using Primer Express software 1.5. Primer and probe sequences were as follows: forward primer, 5′-ACCACTACCAGCAGAACA-3′ (nucleotides 542–559); reverse primer, 5′-GAACTCCAGCAGGACCAT-3′ (nucleotides 655–672); TaqMan Probe, 5′-FAM-AAGACCCCAACGAGAA-TAMRA-3′ (nucleotides 629–644). We used

control reagent mix (PE Applied Biosystems) to amplify 18S rRNA as an internal control, according to the manufacturer's protocol.

For analysis of survivin expression levels, we extracted total RNA as above from tumors treated with MN-NIRF-siSurvivin and control LS174T tumors. We performed RT-PCR as for 9L-GFP tumors. Primer and probe sequences were as follows: forward primer, 5′-GGCCCAGTGTTTCTTCTGCTT-3′ (nucleotides 162–182); reverse primer, 5′-GCAACCGGACGAATGCTTT-3′ (nucleotides 234–252); TaqMan probe, 5′-FAM-AGCCAGATGACGACCCCA TAGAGGAACA-TAMRA-3′ (nucleotides 203–230).

Mice models and treatment with MN-NIRF-siSurvivin. Mice models used in this study included lateral 9L-GFP, 9L-RFP and LS174T tumors. Details on tumor propagation and treatment with MN-NIRF-siSurvivin are provided in **Supplementary Methods**.

MR and optical imaging. We performed *in vivo* MRI on 9L-GFP and 9L-RFP tumor-bearing mice before and 24 h after injection of MN-NIRF-siGFP (10 mg/kg Fe, 440 nmols/kg siRNA) using a 4.7 T GE magnet with a Bruker Biospin Avance console. We imaged mice bearing LS174T tumors in a 9.4T GE magnet with a Bruker Biospin Avance console. We performed *ex vivo* MR imaging of excised tumors on a 14 T vertical bore Bruker/Magnex scanner with a 10-mm internal diameter Bruker volume coil.

For optical imaging, we placed mice into a whole-body animal imaging system (Imaging Station IS2000MM, Kodak), equipped with appropriate band-pass excitation and long-pass emission filters.

Details on MRI and optical imaging parameters and image reconstruction and analysis are provided in **Supplementary Methods**.

Biodistribution. For biodistribution, we intravenously injected mice bearing bilateral 9L-GFP and 9L-RFP tumors ($n = 3$) with ^{125}I-labeled MN-NIRF-siGFP probe (10 mg Fe per kg body weight). After 24 h, we killed the mice, removed and weighed tumors, fluids and organs, and counted organ-associated radioactivity in a gamma-counter. We expressed biodistribution results as the percentage of the injected dose per gram of tissue (% ID/g). All animal experiments were performed in compliance with institutional guidelines and approved by the Subcommittee on Research Animal Care (SRAC) at Massachusetts General Hospital.

Statistical analysis. We expressed data as mean ± s.d. or mean ± s.e.m. where indicated. We analyzed statistical differences by Student's *t*-test (SigmaStat 3.0; Systat Software). We analyzed statistical correlations using Pearson (parametric) test. We considered a value of $P < 0.05$ to be statistically significant.

Note: Supplementary information is available on the Nature Medicine website.

ACKNOWLEDGMENTS

The authors thank J. Moore and P. Pantazopoulos for technical support with animal surgery. Confocal microscopy was performed at the Confocal Microscopy Core at MGH with technical assistance from I.A.Bagayev.

AUTHOR CONTRIBUTIONS

A.M. supervised the project; Z.M. conducted the bioassay, histology and cell biology experiments, and performed the *in vivo* MRI experiments and the *in vivo* and *ex vivo* optical imaging experiments; W.P. performed probe synthesis and characterization of the probe; C.F. performed the *ex vivo* MRI experiments; V.P. conducted the RT-PCR experiments. A.M., Z.M. and W.P. wrote the manuscript.

COMPETING INTERESTS STATEMENT

The authors declare that they have no competing financial interests.

Published online at http://www.nature.com/naturemedicine/
Reprints and permissions information is available online at http://npg.nature.com/reprintsandpermissions

1. Bertrand, J.R. *et al.* Comparison of antisense oligonucleotides and siRNAs in cell culture and *in vivo*. *Biochem. Biophys. Res. Commun.* **296**, 1000–1004 (2002).
2. Brummelkamp, T.R., Bernards, R. & Agami, R. Stable suppression of tumorigenicity by virus-mediated RNA interference. *Cancer Cell* **2**, 243–247 (2002).
3. Xia, H. *et al.* RNAi suppresses polyglutamine-induced neurodegeneration in a model of spinocerebellar ataxia. *Nat. Med.* **10**, 816–820 (2004).
4. Song, E. *et al.* RNA interference targeting Fas protects mice from fulminant hepatitis. *Nat. Med.* **9**, 347–351 (2003).
5. Lewis, D.L., Hagstrom, J.E., Loomis, A.G., Wolff, J.A. & Herweijer, H. Efficient delivery of siRNA for inhibition of gene expression in postnatal mice. *Nat. Genet.* **32**, 107–108 (2002).
6. Layzer, J.M. *et al.* *In vivo* activity of nuclease-resistant siRNAs. *RNA* **10**, 766–771 (2004).
7. Hassani, Z. *et al.* Lipid-mediated siRNA delivery down-regulates exogenous gene expression in the mouse brain at picomolar levels. *J. Gene Med.* **7**, 198–207 (2005).
8. Landen, C.N., Jr. *et al.* Therapeutic EphA2 gene targeting *in vivo* using neutral liposomal small interfering RNA delivery. *Cancer Res.* **65**, 6910–6918 (2005).
9. Takeshita, F. *et al.* Efficient delivery of small interfering RNA to bone-metastatic tumors by using atelocollagen *in vivo*. *Proc. Natl. Acad. Sci. USA* **102**, 12177–12180 (2005).
10. Song, E. *et al.* Antibody mediated *in vivo* delivery of small interfering RNAs via cell-surface receptors. *Nat. Biotechnol.* **23**, 709–717 (2005).
11. Urban-Klein, B., Werth, S., Abuharbeid, S., Czubayko, F. & Aigner, A. RNAi-mediated gene-targeting through systemic application of polyethylenimine (PEI)-complexed siRNA *in vivo*. *Gene Ther.* **12**, 461–466 (2005).
12. Dorn, G. *et al.* siRNA relieves chronic neuropathic pain. *Nucleic Acids Res.* **32**, e49 (2004).
13. Hamar, P. *et al.* Small interfering RNA targeting Fas protects mice against renal ischemia-reperfusion injury. *Proc. Natl. Acad. Sci. USA* **101**, 14883–14888 (2004).
14. Bitko, V., Musiyenko, A., Shulyayeva, O. & Barik, S. Inhibition of respiratory viruses by nasally administered siRNA. *Nat. Med.* **11**, 50–55 (2005).
15. McCaffrey, A.P. *et al.* RNA interference in adult mice. *Nature* **418**, 38–39 (2002).
16. Yano, J. *et al.* Antitumor activity of small interfering RNA/cationic liposome complex in mouse models of cancer. *Clin. Cancer Res.* **10**, 7721–7726 (2004).
17. Chiu, Y.L., Ali, A., Chu, C.Y., Cao, H. & Rana, T.M. Visualizing a correlation between siRNA localization, cellular uptake, and RNAi in living cells. *Chem. Biol.* **11**, 1165–1175 (2004).
18. Moore, A., Medarova, Z., Potthast, A. & Dai, G. *In vivo* targeting of underglycosylated MUC-1 tumor antigen using a multimodal imaging probe. *Cancer Res.* **64**, 1821–1827 (2004).
19. Moore, A., Marecos, E., Bogdanov, A., Jr. & Weissleder, R. Tumoral distribution of long-circulating dextran-coated iron oxide nanoparticles in a rodent model. *Radiology* **214**, 568–574 (2000).
20. Bourrinet, P. *et al.* Preclinical safety and pharmacokinetic profile of ferumoxtran-10, an ultrasmall superparamagnetic iron oxide magnetic resonance contrast agent. *Invest. Radiol.* **41**, 313–324 (2006).
21. Hu-Lieskovan, S., Heidel, J.D., Bartlett, D.W., Davis, M.E. & Triche, T.J. Sequence-specific knockdown of EWS-FLI1 by targeted, nonviral delivery of small interfering RNA inhibits tumor growth in a murine model of metastatic Ewing's sarcoma. *Cancer Res.* **65**, 8984–8992 (2005).
22. Morrissey, D.V. *et al.* Potent and persistent *in vivo* anti-HBV activity of chemically modified siRNAs. *Nat. Biotechnol.* **23**, 1002–1007 (2005).
23. Judge, A.D. *et al.* Sequence-dependent stimulation of the mammalian innate immune response by synthetic siRNA. *Nat. Biotechnol.* **23**, 457–462 (2005).
24. Hornung, V. *et al.* Sequence-specific potent induction of IFN-α by short interfering RNA in plasmacytoid dendritic cells through TLR7. *Nat. Med.* **11**, 263–270 (2005).
25. Zaffaroni, N., Pennati, M. & Daidone, M.G. Survivin as a target for new anticancer interventions. *J. Cell. Mol. Med.* **9**, 360–372 (2005).
26. Massoud, T.F. & Gambhir, S.S. Molecular imaging in living subjects: seeing fundamental biological processes in a new light. *Genes Dev.* **17**, 545–580 (2003).
27. Maeda, H., Fang, J., Inutsuka, T. & Kitamoto, Y. Vascular permeability enhancement in solid tumor: various factors, mechanisms involved and its implications. *Int. Immunopharmacol.* **3**, 319–328 (2003).
28. Zimmer, C. *et al.* Tumor cell endocytosis imaging facilitates delineation of the glioma-brain interface. *Exp. Neurol.* **143**, 61–69 (1997).
29. Harborth, J. *et al.* Sequence, chemical, and structural variation of small interfering RNAs and short hairpin RNAs and the effect on mammalian gene silencing. *Antisense Nucleic Acid Drug Dev.* **13**, 83–105 (2003).
30. Soutschek, J. *et al.* Therapeutic silencing of an endogenous gene by systemic administration of modified siRNAs. *Nature* **432**, 173–178 (2004).
31. Zimmermann, T.S. *et al.* RNAi-mediated gene silencing in non-human primates. *Nature* **441**, 111–114 (2006).
32. Tiscornia, G., Singer, O., Ikawa, M. & Verma, I.M. A general method for gene knockdown in mice by using lentiviral vectors expressing small interfering RNA. *Proc. Natl. Acad. Sci. USA* **100**, 1844–1848 (2003).
33. Tiscornia, G., Tergaonkar, V., Galimi, F. & Verma, I.M. CRE recombinase-inducible RNA interference mediated by lentiviral vectors. *Proc. Natl. Acad. Sci. USA* **101**, 7347–7351 (2004).
34. Haas, J., Park, E.C. & Seed, B. Codon usage limitation in the expression of HIV-1 envelope glycoprotein. *Curr. Biol.* **6**, 315–324 (1996).
35. Moore, A., Marecos, E., Simonova, M., Weissleder, R. & Bogdanov, A., Jr. Novel gliosarcoma cell line expressing green fluorescent protein: a model for quantitative assessment of angiogenesis. *Microvasc. Res.* **56**, 145–153 (1998).